

The Local Bubble and Interstellar Material Near the Sun

P. C. Frisch^{1,*}

¹*Dept. of Astronomy and Astrophysics, University of Chicago, 5640 S. Ellis Ave., Chicago, IL 60637, USA*

(*Author for correspondence, Email: frisch@uchicago.edu)

Abstract. The properties of interstellar matter (ISM) at the Sun are regulated by our location with respect to the Local Bubble (LB) void in the ISM. The LB is bounded by associations of massive stars and fossil supernovae that have disrupted natal ISM and driven intermediate velocity ISM into the LB interior void. The Sun is located in such a driven ISM parcel, which is low density ($< 10^{-24.2}$ g cm⁻³). The Local Fluff has a bulk velocity of ~ 19 km s⁻¹ in the LSR, and an upwind direction at the center of the gas and dust ring formed by the Loop I supernova remnant interaction with the LB. Radiative transfer models give the properties of the Local Interstellar Cloud, LIC, at the heliosphere. The mystery of missing pressure is solved when the ram pressure of the LIC is included in the total LIC pressure. In this case, and if magnetic thermal and cosmic ray pressures are similar in the LIC, the LIC appears to be in pressure equilibrium with the plasma in the local hot bubble.

Keywords: ISM: general, ISM: abundances

1. Introduction

The existence of an area clear of interstellar material around the Sun, now known as the Local Bubble, was discovered as an underdense region in measurements of starlight reddening (Fitzgerald, 1968). Low color excess regions, $E(B - V) < 0.01$ mag,¹ extend to ~ 50 pc in the galactic center hemisphere, and > 100 pc in the interval $l = 180^\circ - 270^\circ$. In the plane of Gould's Belt, the "walls" of the Local Bubble are defined by interstellar material (ISM) associated with star forming regions. At high galactic latitudes the Local Bubble boundaries are defined by interstellar gas and dust displaced by stellar evolution, particularly supernova in the Scorpius-Centaurus Association (SCA). Supernova exploding in pre-existing cavities created by massive star winds displace ISM and the interstellar magnetic field (B_{IS}) into giant magnetized bubbles hundreds of parsecs in extent. The location of the Sun within such a void regulates the interstellar radiation field (ISRF) at the Sun, and the composition and properties of the ISM surrounding the heliosphere.

This paper is in honor of Prof. Johannes Geiss, founder the International Space Sciences Institute (ISSI). Many of the contemporary space topics discussed at ISSI meetings, such as the heliosphere, Local Interstellar Cloud (LIC), cosmic ray acceleration and propagation, and the composition of matter, are influenced by the solar location inside of the Local Bubble. The LIC itself is part of a low density ISM flow, with an upwind direction near the center of Loop I and the Scorpius-Centaurus

¹ $E(B - V) = A_B - A_V$, where $A_{B,V}$ is the attenuation in units of magnitude in the blue (B) and visible (V) bands, respectively.

Association. The flow, with best-fit LSR velocity of 19.4 km s^{-1} , appears to be a break-away fragment of the Loop I superbubble shell surrounding the SCA, which has expanded into the low density interior of the Local Bubble (§2.1, Frisch, 1981; Frisch, 1995; Breitschwerdt et al., 2000).

2. Origin and Boundaries of the Local Bubble

2.1. ORIGIN

The Local Bubble void has been created by star formation processes that have occurred during the past 25–60 Myrs in the corotating region of the Milky Way Galaxy near the solar location of today. About 26–60 Myrs ago a blast wave evacuated a low density region at the present location of the Sun, and compressed surrounding molecular clouds to initiate the formation sequence of the massive OB stars now attributed to Gould’s Belt. Gould’s Belt denotes the system of kinematically related massive OB stars within $\sim 500 \text{ pc}$ of the Sun, which form a localized plane tilted by $\sim 18^\circ$ with respect to the galactic plane. The center of Gould’s Belt is 104 pc from the Sun towards $\ell=180^\circ$, and with an ascending node longitude of 296° (Grenier, 2004). The Sun is moving away from the center of Gould’s Belt, and is closest to the Scorpius-Centaurus rim. Since the formation of Gould’s Belt, the Sun has traveled hundreds of parsecs through the LSR, and the LSR has completed $\sim 10\% - 25\%$ of its orbit around the galactic center. Molecular clouds disrupted by the initial blast wave now rim Gould’s Belt. Epochs of star formation in the Scorpius-Centaurus Association during the past 1–15 Myrs further evacuated the Local Bubble void, and displaced ISM from the SCA into giant nested H° shells (de Geus, 1992). One of these shells, Loop I (or the North Polar Spur), was formed by a recent supernova ($< 1 \text{ Myrs}$ ago) and is an intense source of polarized synchrotron and soft X-ray (SXR) emission. A ring-like shadow, caused by foreground ISM, is seen in the Loop I SXR emission. The origin of this ring has been suggested to be the result of Loop I merging with the separate Local Bubble (e.g. Egger and Aschenbach, 1995). The LSR upwind direction of the Local Fluff² is at the center of this ring, and polarization data show that the ring is a magnetic loop (see Fig. 1).

Supernova associated with the formation of the Lower Centaurus Crux subgroup of SCA (11-12 Myrs ago) appear the most likely events to have created the Local Bubble as we see it today (Frisch, 1995; Maiz-Appellaniz, 2001). Among the overlapping superbubbles that form a $\sim 1 \text{ kpc}$ long hole in H° in the galactic plane at the solar location are the North Polar Spur (Loop I), Eridanus Loop, Orion Nebula, Gum Nebula, Perseus Cluster and Collinder 121 (Heiles, 1998).

² This direction is in the local standard of rest, LSR, which is obtained by correcting heliocentric velocity vectors for the solar apex motion. The Standard solar apex velocity of 19.7 km s^{-1} , towards $\ell=57^\circ$ and $b=22^\circ$ is used. The Local Fluff LSR upwind is $\ell, b=331^\circ, -5^\circ$, with LSR velocity -19.4 km s^{-1} .

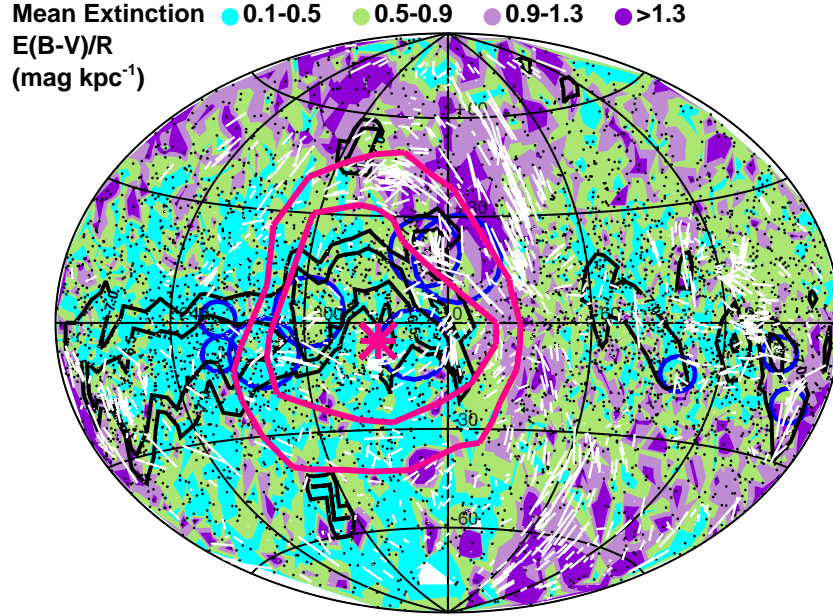


Figure 1. Mean extinction, $E(B - V)/R$, for stars at R kpc, for $R < 0.5$. Black contours show the integrated stellar radiation at 1565 Å measured by the TD-1 satellite (Gondhalekar et al., 1980). Contours indicate flux levels of 10^{-7} and $10^{-6.5}$ ergs cm $^{-2}$ s $^{-1}$ Å $^{-1}$ sterad $^{-1}$. Polarization data for stars within 500 pc of the Sun are plotted as white bars (Heiles 2000). Pink contours show the ring that may be formed by the Loop I supernova remnant interaction with the Local Bubble (Egger and Aschenbach, 1995). The pink asterisk indicates the LSR upwind direction of the Local Fluff (see text). Stellar reddening data are the same as for Fig. 2. Blue circles show stellar OB associations within 500 pc of the Sun. An Aitoff projection is used, with the galactic center at the center of the plot, and ℓ increasing to the right. Note that the ISM density is very low out to 500 pc in the third/fourth galactic quadrants, $\ell = 180^\circ - 270^\circ$, particularly towards low galactic latitudes.

2.2. BOUNDARIES

The locations of the Local Bubble boundaries have been diagnosed with a range of different ISM markers, including color excess (Lucke, 1978), ultraviolet observations of interstellar H $^{\circ}$ lines in hot stars (York & Frisch, 1983, Paresce, 1984), radio H $^{\circ}$ 21-cm and optical Na $^{\circ}$ data (Vergely et al., 2001), extreme ultraviolet (EUV, $\lambda < 912$ Å) emission of white dwarf and M-stars (Warwick, 1993), measurements of polarization of starlight (Leroy, 1999), and the trace ionization species Na $^{\circ}$ (Sfeir et al., 1999, Lallement et al. 2003). These studies differ in sampling densities and spatial smoothing methods. Each marker is an imprecise tracer of the total ISM mass density, ρ_{ISM} , since the ISM is highly inhomogeneous over the scale lengths

of the Local Bubble, and this affects mean conversion factors between the marker data and ρ_{ISM} . I focus here on the reddening data.

An accessible measure of starlight reddening is color excess, $E(B - V)$, which measures the differential extinction of starlight in the blue versus visual bands, and is sensitive to interstellar dust grains (ISDG) of radii $a \sim 0.20 \mu\text{m}$. Interstellar gas and dust are well mixed, so that the Local Bubble walls found from $E(B - V)$ data in principle will be consistent with the locations found from gas markers. The exception is that dust is found in both neutral and ionized regions, while the commonly available gas markers (H° , Na°) are weighted towards neutral regions.

Grains and gas are well mixed partly because both populations couple to the interstellar magnetic field (B_{IS}) in cold and warm clouds. In cold clouds with density $n(\text{H})=100 \text{ cm}^{-3}$ and temperature $T \sim 100 \text{ K}$, the $a \sim 0.2 \mu\text{m}$ dust grain with density 2 g cm^{-3} will sweep up its own mass in gas in $\sim 0.08 \text{ Myrs}$. If the same grain has charge $Z=20$, the gyrofrequency for a magnetic field of strength $B=2.5 \mu\text{G}$ is $\sim 1/3300 \text{ yrs}$. For a warm neutral cloud ($n(\text{H}) \sim 0.25 \text{ cm}^{-3}$, $T \sim 6300 \text{ K}$), the grain accumulates its own mass in $\sim 4 \text{ Myrs}$. In both cloud types, grains couple to B_{IS} . Gas also couples to B_{IS} , since elastic collisions couple neutrals and ions over time-scales of years, and minimum ionization levels of $\sim 10^{-4}$ bind gas to B_{IS} (Spitzer, 1978).

The walls of the LB in the galactic plane are shown in Fig. 2, based on $E(B - V)$ data that have been converted to $N(\text{H})$ using $N(\text{H})/E(B - V) \sim 5.8 \times 10^{21} \text{ cm}^{-2} \text{ mag}^{-1} \text{ K}$ (Bohlin et al., 1978). A threshold value of $E(B - V) > 0.04 \text{ mag}$ (or $\log N(\text{H}) > 20.4 \text{ cm}^{-2} \text{ dex}$) is used. For cloudy sightlines (high mean $E(B - V)$ values), the fraction of the H atoms in H_2 (f_{H_2}) rises above $\sim 1\%$ at this threshold. The old term “intercloud” refers to low column density sightlines with relatively little H_2 ($f_{\text{H}_2} < 1\%$). There is an obvious deficit of dust within $70 - 100 \text{ pc}$ for all galactic longitudes. In the third and fourth galactic quadrants ($\ell = 180^\circ \rightarrow 270^\circ \rightarrow 360^\circ$, QIII, QIV) the deficit extends to distances beyond 200 pc .

The $E(B - V)$ data in Fig. 2 represent the cumulative color excess towards 3000 O, B, and A stars, within $\sim 200 \text{ pc}$ of the Sun and 45° of the galactic plane. The $E(B - V)$ values are determined from photometric data in the Hipparcos catalog (Perryman et al., 1997). Molecular clouds of CO and H_2 are also shown, and are plotted as filled red circles (Dame et al., 2001). Well-known molecular clouds at the rim of the Local Bubble include dust in Scorpius ($\ell \sim 350^\circ$, $d \sim 120 \text{ pc}$), Taurus ($\ell \sim 160^\circ$, $d \sim 120 \text{ pc}$), and Chameleon ($\ell \sim 305^\circ$, $b \sim -15^\circ$, $d \sim 165 \text{ pc}$).

In Fig. 1, the reddening per unit distance, $E(B - V)/r$, is plotted on an Aitoff projection for stars within 500 pc . The lowest mean densities ISM between longitudes of 210° and 360° are evident. Star groups (blue circles) in the low density sightlines include Sco OB2, Vela OB2, and Trumpler 10 (de Zeeuw et al., 1999). The lowest mean densities in this data set, outside of the Local Fluff, correspond to $0.006 \text{ atoms cm}^{-3}$. At the galactic poles, $|b| > 75^\circ$, the edges of the Local Bubble, where $E(B - V) > 0.05 \text{ mag}$ (or $\log N(\text{H}) > 20.50 \text{ cm}^{-2}$), are at $80\text{--}95 \text{ pc}$ towards both the north and south poles.

The relation between interstellar dust ($E(B - V)$) and hydrogen column density ($N(\text{H}) = N(\text{H}^0) + 2N(\text{H}_2)$) varies by $\sim 15\%$ between sightlines with low and high fractions of H_2 (Bohlin et al., 1978). This variation does not affect this plot. The difference arises from variations in grain sizes between cloudy and intercloud sightlines, and perhaps also partly from an inhomogeneous 912-1108 Å radiation field capable of photodissociating H_2 . The $\lambda \sim 1565$ Å radiation field depends on location with respect to the Local Bubble walls (§4.1), and the 1000 Å field should behave in a similar fashion.

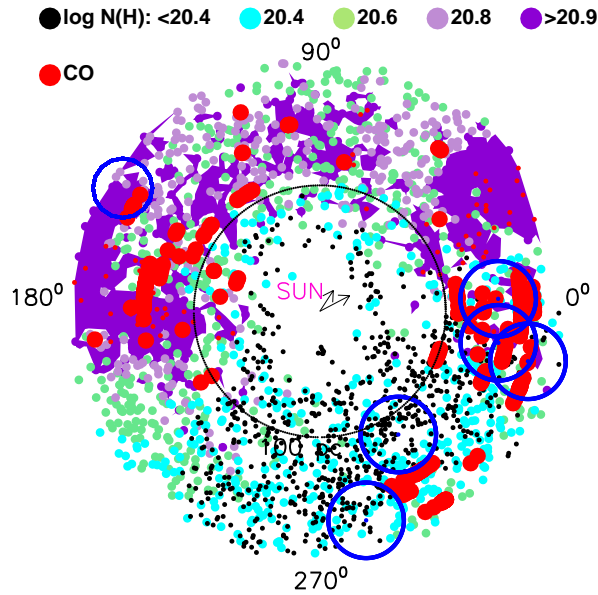


Figure 2. The distribution of interstellar matter surrounding the Local Bubble void. Molecular clouds of CO and H_2 are plotted as red symbols (Dame et al. 2000). The colored dots show the column density of interstellar hydrogen, $N(\text{H}) = N(\text{H}^0) + N(\text{H}^+) + 2N(\text{H}_2)$, in front of 3000 OBA stars. Column densities are based on dust reddening determined from $E(B - V)$, where $E(B - V)$ is calculated from the photometric data in the Hipparcos catalog, and $E(B - V)$ is averaged over stars in a sector with angular width of $\pm 13^\circ$, and overlapping distance uncertainties. The gas-to-dust ratio found from ultraviolet data is used, $N(\text{H})/E(B - V) = 5.8 \times 10^{21} \text{ cm}^{-2} \text{ mag}^{-1}$. The amount of $N(\text{H})$ will be overestimated for low column densities, $N(\text{H}) < 10^{20}$, by this relation (Bohlin et al. 1978). Sightlines with $N(\text{H}) > 10^{20.9} \text{ cm}^{-2}$ have been plotted with filled purple contours. The arrows show two different values for the direction of the Sun's motion through the local standard of rest, with the longer arrow ($v = 19.5 \text{ km s}^{-1}$) indicating the standard value. Blue circles represent OB associations within 200 pc of the Sun. Objects within $\pm 45^\circ$ of the galactic plane, and 200 pc of the Sun, are plotted. The circle shows distances of 100 pc.

3. Loop I and the Local Magnetic Field

3.1. LOOP I AND THE HIGH-LATITUDE LIMITS OF THE LOCAL BUBBLE

Above the galactic plane in the galactic-center hemisphere, $b > 20^\circ$, the LB walls are established by neutral gas of the Loop I superbubble. The interval $\ell \sim 270^\circ \rightarrow 50^\circ$ is encircled by nested shells of gas and dust. Loop I is $\sim 80^\circ$ in radius and centered 120 pc away at $\ell = 320^\circ$, $b = 5^\circ$ for the neutral gas (Berkhuijsen 1971; Heiles, 1998; de Geus, 1992). The central regions of these shells are deficient in ISM, creating the extension of the Local Bubble towards $\ell \sim 340^\circ$ (Fig. 2).

3.2. MAGNETIC FIELD

Loop I dominates the magnetic field structure near the Sun, and is a source of intense radio continuum and soft X-ray emission. The Loop I magnetic field is traced by polarized synchrotron emission, starlight polarization caused by magnetically aligned dust grains, Faraday rotation, and Zeeman splitting of the H° 21-cm line. Fig. 1 shows the starlight polarization vectors (from Heiles, 2000). Magnetically aligned ISDGs are birefringent at optical wavelengths, with lower opacities found for the polarization component parallel to B_{IS} . The Loop I magnetic field direction is shown by the gradient in the rotation angle of the optical polarization vectors. The gradient follows the interaction ring shape. Comparisons between the optical polarization data and synchrotron emission, where polarizations are perpendicular to B_{IS} , indicate that B_{IS} is nearly in the plane of the sky in Loop I (Berkhuijsen, 1972, Heiles & Crutcher, 2005).

The closest measured B_{IS} strengths are towards Loop I. Heiles et al. (1980) found a volume averaged field strength of $B_{IS} \sim 4 \mu\text{G}$ in a tangential direction through the shell (extending $\sim 70 \pm 30$ pc towards $\ell = 34^\circ$, $b = 42^\circ$). Faraday rotations of extragalactic radio sources indicate that the parallel component (to the sightline) of the magnetic field in Loop I is very small, with an average value of $B_{||} = 0.9 \pm 0.3 \mu\text{G}$ from rotation measure data (Frick et al., 2001). In the neutral gas of the shell, magnetic pressure is dominant, and in the ionized gas producing the radio continuum emission, the magnetic, gas, and cosmic ray pressures are all significant. Loop I is a decelerated shock generated by sequential star formation in SCA (de Geus, 1992), and the magnetic field strength is set by flux-freezing.

3.3. THE LIC AND THE MAGNETIC FIELD AT THE SUN

The LIC is very low density, $n(\text{H}) \sim 0.25 - 0.30 \text{ cm}^{-3}$. Magnetic fields in high density ISM show evidence of flux freezing, however B_{IS} in low density ISM is not correlated with the density (Heiles & Crutcher, 2005). Pulsar dispersion measures indicate that the uniform component of the magnetic field near the Sun is $B_{IS} \sim 1.4 \mu\text{G}$, with correlation lengths of ~ 100 pc (Rand & Kulkarni, 1989). In general, structure functions created from data on radio continuum polarization

near 21 cm show that magnetoionized structures in interarm sightlines must be very large (e.g. ~ 100 pc, Haverkorn et al., 2006). This would indicate that the uniform B_{IS} component is appropriate for the low density (similar to interarm) region around the Sun.

The physical conditions of the LIC have been modeled by developing a series of radiative transfer models that are constrained by observations of He° and pickup ion and anomalous cosmic ray data inside of the heliosphere, and observations of the LIC towards ϵ CMa. These models are discussed in detail in Slavin and Frisch (this volume, and 2007, hereafter SF07a,b). The best of these models give $n(\text{H}^\circ) = 0.19 - 0.20 \text{ cm}^{-3}$, $n(\text{e}) = 0.07 \pm 0.02 \text{ cm}^{-3}$, $n(\text{He}^\circ) = 0.015 \text{ cm}^{-3}$, for cloud temperatures ~ 6300 K. If the magnetic and gas pressures are equal in the LIC, then the LIC field strength is $B_{\text{LIC}} \sim 2.8 \mu\text{G}$. This value is consistent with the interface magnetic field strength of $2.5 \mu\text{G}$, required by the best model (model 26). However, it is somewhat above the strength of the uniform component of B_{IS} . Since the ISM flow past the Sun has an origin associated with the breakaway of a parcel of ISM from the Loop I magnetic superbubble, perhaps B_{IS} at the Sun is stronger and perturbed compared to the uniform field, but at lower pressure than the confined parts of the Loop I bubble.

Very weak interstellar polarization caused by magnetically aligned dust grains has been observed towards stars within ~ 30 pc (Tinbergen, 1982). The polarization was originally understood to arise in the Local Fluff, since the polarization region coincides with the upwind direction of the flow where column densities are highest. More recently, the polarization properties were found to have a systematic relation to ecliptic position. The region of maximum polarization is found to be located at ecliptic longitudes that are offset by $\sim +35^\circ$ from the large dust grains flowing into the heliosphere (Frisch et al., 1999), and from the gas upwind direction. These polarization data are consistent with the interpretation that polarizing grains are trapped in B_{IS} as it drapes over the heliosphere (Frisch, 2005, 2006). When magnetically prealigned (by B_{IS}) ISDGs approach the heliosphere, the gas densities are too low to collisionally disrupt the alignment. The result is that the polarization should indicate the direction of B_{IS} at the heliosphere. If the alignment mechanism is sufficiently rapid, the alignment direction will also adjust to the interstellar magnetic field direction as it drapes over the heliosphere. Although this interpretation of the polarization data is not confirmed, it fits the physics of dust grains interacting with the heliosphere. Small charged grains such as those that polarize starlight ($a < 0.2 \mu\text{m}$) couple to B_{IS} and are excluded from the heliosphere, while large grains enter the heliosphere where they are measured by various spacecraft (see Krueger, this volume). The characteristics of such polarization may vary with solar cycle phase.

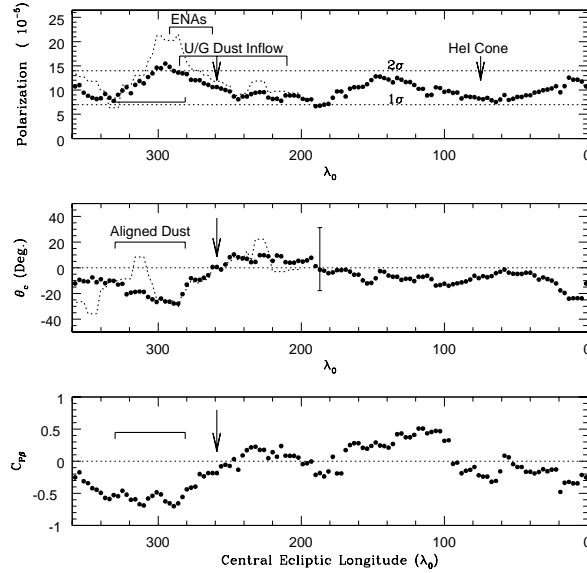


Figure 3. Interstellar polarizations towards nearby stars (Tinbergen, 1982, data) compared to the ecliptic position of the star. A systematic enhancement of the polarization strength is found at an offset of $\sim 30^\circ$ compared to the inflowing gas and large dust grain direction. Top: The average polarization P for stars with $|\beta| < 50^\circ$ is plotted as dots, and for stars with $|\beta| < 20^\circ$ as a dashed line. Data are averaged over $\pm 20^\circ$ in ecliptic longitude, λ . The direction of maximum P is shifted by $\sim 25^\circ - 40^\circ$ from the upwind direction of the large interstellar dust grains detected by Ulysses/Galileo (Frisch et al., 1999). The upwind gas and large-grain directions differ by $< 5^\circ$. Middle: The averaged polarization position angle in celestial coordinates, Θ_e . In the region of maximum polarization, $\lambda \sim 280^\circ \rightarrow 310^\circ$, the grains show consistent position angles. Bottom: The correlation coefficient between P (top) and β is shown as a function of the ecliptic longitude. The strongest polarization is found at negative ecliptic latitudes. For more details see Frisch (2005, 2006).

4. Radiation Environment of the Local Bubble

4.1. INHOMOGENEOUS RADIATION FIELD AND LOCAL FLUFF IONIZATION

The interstellar radiation field (ISRF) is a key parameter for understanding the physical properties of the LIC and Local Fluff. The sources of the ISRF at the Sun include plasma emission from the Local Bubble interior and supernova remnants, stellar radiation, including from hot white dwarf stars, and emission from a conductive interface between the local fluff and the hot plasma. The spectrum of this field at the surface of the LIC is shown in Slavin and Frisch (this volume).

The spectrum of the ISRF is inhomogeneous because of the energy-dependent opacity of the ISM. For instance, radiation with $\lambda < 912$ (or 584 Å) determines the ionizations of H (or He). Energetic photons capable of ionizing H^0 (or He^0)

require $N(\text{H}^\circ) \sim 17.2$ (or 17.7) cm^{-2} to reach an opacity $\tau \sim 1$. The dependence of $\tau_{912\text{\AA}}/\tau_{504\text{\AA}}$ on $N(\text{H}^\circ)$ drives the need for LIC photoionization models to determine the heliosphere boundary conditions. Stars within ~ 10 pc (e.g. Wood et al. 2005) show local column density variations of $\log N(\text{H}^\circ) \sim 17.07 - 18.22$ cm^{-2} dex (assuming $\log D/H = -4.7$). This yields a range locally of $\tau_{912\text{\AA}} = 0.7 - 10.5$, and shows that ionization must vary between the individual cloudlets comprising the Local Fluff. This variation is confirmed by N^+ data, which are excellent tracers of H^+ through charge-exchange. Stars within 70 pc show $\text{N}^+/\text{N}^\circ \sim 0.1 - 2$ (SF07a,b). Our LIC radiative transfer models indicate that in the LIC H° ionization provides $\sim 66\%$ of the cloud heating, and the LIC is $\sim 20 - 30\%$ ionized (SF07a,b).

Another example of the inhomogeneous ISRF is provided by the photon flux at $\lambda \sim 1565$ Å, which TD-1 satellite data show depends on position in the Local Bubble (Gondhalekar et al., 1980). The ISRF at $\lambda 1565$ Å is dominated by hot stars, B or earlier. Radiation at $\lambda \leq 1620$ Å regulates the photoionization rate of interstellar Mg° , and is an important parameter for the $\text{Mg}^+/\text{Mg}^\circ$ diagnostic of the interstellar electron density. The ISDG albedo at $\lambda \sim 1565$ Å is ~ 0.5 . Fig. 1 shows the flux of 1565 Å photons at the Sun, plotted as black contours. This flux is dominated by starlight, and the brightest regions of the sky at 1565 Å are in the third and fourth galactic quadrants, $\ell \sim 180^\circ - 360^\circ$, where the mean extinction in the interior of the Local Bubble is low, $E(B - V)/d < 0.4$ mag kpc $^{-1}$.

The fact that the 1565 Å radiation field is enhanced in QIII and QIV is relevant to our understanding of the more energetic photons associated with the soft X-ray background (SXRb). Isolated bright SXRb regions are seen, such as the Orion-Eridanus and Loop I enhancements, however no regional enhancement in the SXRb flux is seen corresponding to the bright $\lambda 1565$ Å regions.

4.2. DIFFUSE SOFT X-RAY BACKGROUND

The diffuse soft X-ray background (SXRb) is significant both as an ionizing and heating radiation field, and as a fossil that traces the formation mechanism for the Local Bubble.

The spectrum of the soft X-ray background (SXRb) emission found from broadband sounding rocket observations at energies $\sim 0.08 - 0.2$ keV revealed an excess of count rates at low energies in the galactic plane, compared with the emission expected from a $T \sim 10^6$ K plasma. This effect was interpreted as indicating a local X-ray plasma with less than $\sim 7 \times 10^{18}$ cm^{-2} of foreground hydrogen (Juda et al., 1991). Fast-forwarding to the present, the LB contributions to the SXRb have been determined from broadband measurements by ROSAT (0.18 – 0.3 keV), and the XMM Newton spectra of dark clouds acquired to isolate the LB flux from foreground and background contaminations (e.g. Bellm and Vaillancourt, 2005, Henley et al. 2007). The SXRb spectrum includes contributions from an absorbed halo and extragalactic component, local supernova remnants such as Loop I which dominates the northern hemisphere sky, and the Local Bubble component. A significant

contaminant to the SXR data is solar wind emission created by charge-exchange (CEX) between the solar wind and neutral interstellar or geocoronal gas (Robertson and Cravens, 2003). The solar wind spectrum is dominated by emission lines from C^{+++} , O^{+6} , O^{+7} , Ne^{+8} , and Mg^{+10} with energies 0.37–1.35 keV (Snowden et al., 2004). Robertson and Cravens (2003) have modeled the contributions of heliospheric charge exchange to the SXR measured by ROSAT, and concluded that $\sim 50\%$ of the SXR in the galactic plane, and $\sim 25\%$ at high latitudes, can be attributed to charge exchange between the solar wind and interstellar neutrals. Bellm and Vaillancourt (2005) compared SXR fluxes observed by ROSAT with sounding rocket data, and concluded that depleted abundances in the LB plasma are required to achieve consistency between the various sets of data. The component of the SXR that does not anticorrelate with $N(H^o)$ limits the contribution of solar wind/ H^o charge-exchange. Bellm and Vaillancourt found that at least 34% of the local contribution in the galactic plane must arise from the LB plasma, based on an upper limit to the CXE flux (see Lallement, this volume), which rises to $> 50\%$ if the CXE fluxes from Robertson and Cravens (2003) are used.

Henley et al. (2007) have obtained XMM Newton spectra on and off a dark cloud, allowing removal of foreground heliospheric contributions; they employed a plasma emission code that relies on recent results on the solar composition (Asplund, this volume) as a template for the plasma composition. They find that for a LB cavity radius of 100 pc, the LB plasma has $n(e)=0.013\text{ cm}^{-3}$, pressure $2.9 \times 10^4\text{ cm}^{-3}\text{ K}$, a cooling time of 17 Myrs, and a sound-crossing time of 1.2 Myrs.

Surprisingly, the LB plasma may be in pressure equilibrium with the LIC, if the LIC ram pressure is considered. The Slavin and Frisch radiative transfer models of the LIC (this volume) indicate the total LIC density is $n(H) \sim 0.26\text{ atoms cm}^{-3}$, and $n(e) \sim 0.07\text{ cm}^{-3}$, for $T = 6300\text{ K}$ and $H/He=10$. If gas thermal, magnetic, and cosmic ray pressures are approximately equal, this gives a static LIC pressure of $\sim 6600\text{ cm}^{-3}\text{ K}$. However the LIC moves by $\sim 20.7\text{ km s}^{-1}$ through the LSR, where the LB plasma should be at rest. If the LIC ram pressure is included, the total LIC pressure is $\sim 2.5 \times 10^4\text{ cm}^{-3}\text{ K}$, which is quite close to the modeled plasma pressure. Including the LIC ram pressure evidently removes the longstanding mystery about the pressure equilibrium between the LIC and LB plasma.

5. The LIC and the ISM Flow Past Sun

5.1. KINEMATICS OF LOCAL FLUFF

The LIC is part of an ISM flow, that has been denoted the Local Fluff, or Cluster of Local Interstellar Clouds (CLIC). The best fitting flow vector for ISM within 31 pc is $-28.1 \pm 4.6\text{ km s}^{-1}$, from the direction $\ell = 12.4^\circ$, $b = 11.6^\circ$ (heliocentric rest frame, Frisch et al. 2002). The upwind direction in the LSR is towards the center

of Loop I (§2.1). The flow is decelerating; in the rest frame of the flow velocity, the fastest components in the upwind and downwind directions are blueshifted by over 10 km s^{-1} . Individual clouds are present in the flow, including the LIC, the “G-cloud” within 1.3 pc of the Sun in the upwind direction, and the Apex cloud that is within 5 pc of the Sun in the upwind direction and extending towards $\ell \sim 30^\circ$. These cloudlets have virtually the same upwind directions, to within $\sim \pm 10^\circ$, indicating a common origin for the cloudlets comprising the Local Fluff. Alternate interpretations of the Local Fluff kinematics have parsed the flow into many spatially extended components, based on velocity and temperature (Linsky, this volume). However, velocity components towards stars in the sidewind direction do not clearly distinguish between individual clouds because of velocity blending.

5.2. INTERSTELLAR ABUNDANCES

The abundance pattern of elements in interstellar gas is characterized by abundances that decrease with increases in the mean gas density ($\langle n(\text{H}) \rangle$) or elemental condensation temperature (T_{cond}). Most depletion studies are based on long sightlines with blended velocity components. Our LIC radiative transfer models derive elemental abundances corrected for ionization, for a single low density cloud in space (SF07a,b). For the best models in SF07b, LIC abundances are O/H=295–437 ppm, compared to solar abundances 460 ppm (Asplund, this volume), and N/H=40–66 ppm, compared to solar values 61 ppm. The LIC S/H ratios are 14–22 ppm, compared to solar values 14 ppm. If the LIC has a solar composition, as indicated by anomalous cosmic ray data for ^{22}Ne and ^{18}O (Cummings, this volume), then Asplund solar abundances are preferred over earlier values. Carbon is found to be overabundant by a factor of ~ 2.6 compared to solar, which helps maintain the LIC cloud temperature near the observed temperature of 6300 K through C fine-structure cooling. The C-abundance anomaly appears to be due to the destruction of carbonaceous grains by interstellar shocks. The carbon overabundance is consistent with the deficit of small carbonaceous grains causing the 2200 Å bump and far ultraviolet rise in the ultraviolet extinction curves in some regions.

Acknowledgements

This work was supported by NASA grants NNG05GD36G, NNG06GE33G, and NAG5-13107. The Hipparcos data-parsing tool was developed by Prof. Philip Chi-Wing Fu, under the auspices of NASA grant NAG5-11999.

References

- Bellm, E. C. & Vaillancourt, J. E. 2005, *ApJ*, 622, 959
 Bohlin, R. C., Savage, B. D., & Drake, J. F. 1978, *ApJ*, 224, 132

- Breitschwerdt, D., Freyberg, M. J., & Egger, R. 2000, *A&A*, 361, 303
- Dame, T. M., Hartmann, D., & Thaddeus, P. 2001, *ApJ*, 547, 792
- de Geus, E. J. 1992, *A&A*, 262, 258
- de Zeeuw, P. T., Hoogerwerf, R., de Bruijne, J. H. J., Brown, A. G. A., & Blaauw, A. 1999, *AJ*, 117, 354
- Egger, R. J. & Aschenbach, B. 1995, *A&A*, 294, L25
- Fitzgerald, M. P. 1968, *AJ*, 73, 983
- Frick, P., Stepanov, R., Shukurov, A., & Sokoloff, D. 2001, *MNRAS*, 325, 649
- Frisch, P. C. 1995, *Space Sci. Rev.*, 72, 499
- Frisch, P. C. 2005, *ApJ*, 632, L143
- Frisch, P. C. 2006, *ApJ*, submitted
- Frisch, P. C., Dorschner, J. M., Geiss, J., et al. 1999, *ApJ*, 525, 492
- Frisch, P. C., Grodnicki, L., & Welty, D. E. 2002, *ApJ*, 574, 834
- Frisch, P. C. & York, D. G. 1983, *ApJ*, 271, L59
- Gondhalekar, P. M., Phillips, A. P., & Wilson, R. 1980, *A&A*, 85, 272
- Grenier, I. A. 2004, *ArXiv Astrophysics e-prints*
- Haverkorn, M., Gaensler, B. M., Brown, J. C., et al. 2006, *ApJ*, 637, L33
- Heiles, C. 1998, *ApJ*, 498, 689
- Heiles, C. 2000, *AJ*, 119, 923
- Heiles, C., Chu, Y. ., Troland, T. H., Reynolds, R. J., & Yegingil, I. 1980, *ApJ*, 242, 533
- Heiles, C. & Crutcher, R. 2005, *ArXiv Astrophysics e-prints*
- Henley, D. B., Shelton, R. L., & Kuntz, K. D. 2007, *ArXiv Astrophysics e-prints*
- Juda, M., Bloch, J. J., Edwards, B. C., et al. 1991, *ApJ*, 367, 182
- Lallement, R., Welsh, B. Y., Vergely, J. L., Crifo, F., & Sfeir, D. 2003, *A&A*, 411, 447
- Leroy, J. L. 1999, *A&A*, 346, 955
- Lucke, P. B. 1978, *A&A*, 64, 367
- Maíz-Apellániz, J. 2001, *ApJ*, 560, L83
- Paresce, F. 1984, *AJ*, 89, 1022
- Perryman, M. A. C. 1997, *A&A*, 323, L49
- Rand, R. J. & Kulkarni, S. R. 1989, *ApJ*, 343, 760
- Robertson, I. P. & Cravens, T. E. 2003, *Journal of Geophysical Research (Space Physics)*, 108, 6
- Sfeir, D. M., Lallement, R., Crifo, F., & Welsh, B. Y. 1999, *A&A*, 346, 785
- Slavin, J. D. & Frisch, P. C. 2007, *A&A*, in preparation
- Snowden, S. L., Collier, M. R., & Kuntz, K. D. 2004, *ApJ*, 610, 1182
- Spitzer, L. 1978, *Physical Processes in the Interstellar Medium* (Newrk: John Wiley & Sons, Inc.)
- Tinbergen, J. 1982, *A&A*, 105, 53
- Vergely, J.-L., Freire Ferrero, R., Siebert, A., & Valette, B. 2001, *A&A*, 366, 1016
- Warwick, R. S., Barber, C. R., Hodgkin, S. T., & Pye, J. P. 1993, *MNRAS*, 262, 289
- Wood, B. E., Redfield, S., Linsky, J. L., Müller, H.-R., & Zank, G. P. 2005, *ApJS*, 159, 118